Electronic Supplementary Material (ESI) for RSC Advances.

Nanostructure and pore size control of template-free synthesised mesoporous magnesium carbonate

By *Ocean Cheung, Peng Zhang, Sara Frykstrand, Haoquan Zheng, Taimin Yang, Marco Sommariva, Xiaodong Zou and Maria Strømme**

Supporting information

Drug loading and release: The chemical structure of ITZ is shown in Figure S1 while Table S1 summarizes some important general properties of the drug.

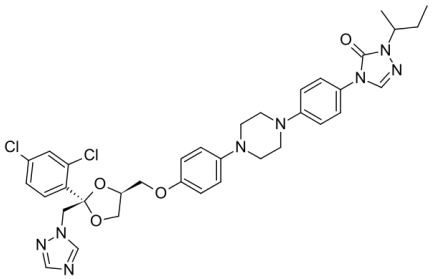

Figure S1. Chemical structure of itraconazole.

Table S1. General properties of itraconazole.

Molecular weight	705.6 g/mol
cLog P	6.2
pKa	3.7
Melting point	438 -442 K
Solubility in water (pH=7)	1 ng/ml
Solubility in gastric fluid (pH=1.2)	4 µg/ml

Data obtained from Ref. [5].

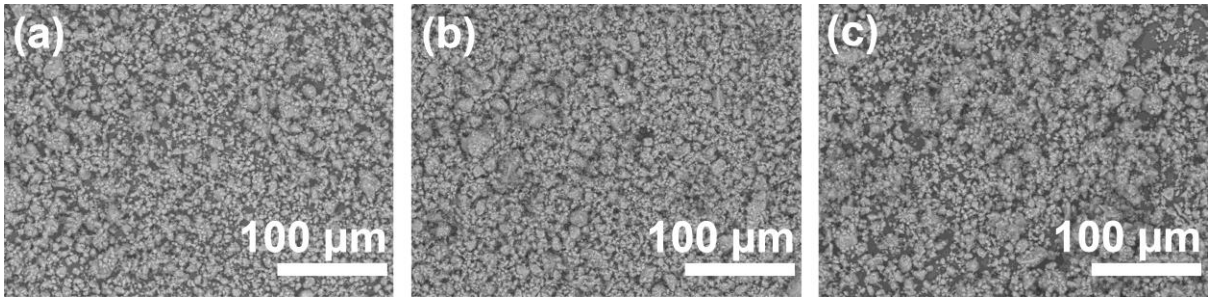

Figure S2. Scanning electron micrograms of ITZ loaded (and grounded) transparent MMC particles with a) 5.1 nm average pore diameter (sample E), b) 13 nm average pore diameter

Oxide content of transparent MMC powder

Figure S3 shows the TGA response of the transparent MMC powder and Table S2 summarizes the MgO content of the transparent powder as determined by CHN analysis, ICP-OES and TGA. The material contained about 14-18 wt.% MgO (and ~ 82-86 wt.% $MgCO_3$) as determined by CHN analysis, ICP-OES and TGA.

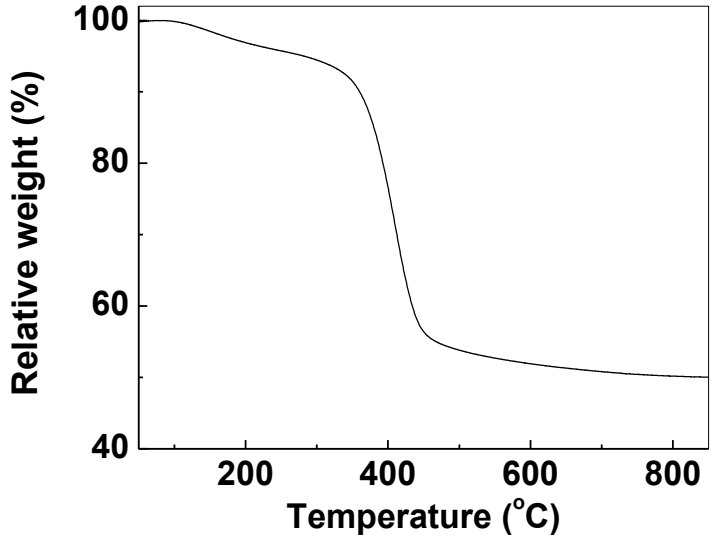

Figure S3. Thermogravimetric curve of transparent MMC powder, the sample weight at 350 °C and 500 °C were used to back-calculate the MgO content of the starting material. The calculated oxide content using the TGA data was ~ wt.13.8%.

Table S2. Elemental composition and MgO content (from CHN/ICP-OES and TGA) of the transparent MMC, oxygen analysis was not possible using ICP due to the high metal. content

	C	**H**	**N**	**Mg**	**MgO wt.% (from CHN/ICP)**	**MgO wt.% (from TGA)**
wt. %	10.80	0.28	<0.01	26.2	17.6	13.8

The difference in the MgO content deduced by elemental analysis and TGA could be due to various reasons. Firstly, elemental analysis was unable to determine oxygen content due to the high metal content indicated. Therefore, in the calculations using both sets of data (elemental analysis and TGA), we assumed that the magnesium present in the transparent powder exists only as MgO and $MgCO_3$. In this case, the oxygen content of the transparent powder was back-calculated using the TGA data to be 60.7 wt.%, which was comparable to the value deduced using the elemental analysis data obtained; 62.7 wt.% (assuming that no elements other than C, H, O and Mg were present in the sample). Secondly, the presence of H (0.28 wt.%) from the CHN analysis suggested that a small amount of hydrogenated species existed in the transparent powder, possibly as surface $Mg(HCO_3)_2$, $Mg(OH)(HCO_3)$ or adsorbed water. The presence of OH groups could be detected using IR spectroscopy (discussed in main text) but could not be quantitatively accounted for using the techniques adopted here. These species may create a small error in the MgO content calculated using TGA, and were most probably responsible for the difference in the elemental analysis and TGA calculated MgO content of the transparent powder. Despite the uncertainties, it was clear that the MgO content of the transparent powder was around 13 – 20 wt.%. Note that on the TGA curve (Figure S3), the few wt.% drop below 250 °C was related to adsorbed water during the handling of the sample before the analysis, as the sample was already dried at 250 °C before the measurement.

High resolution transmission electron microscopy (HRTEM)

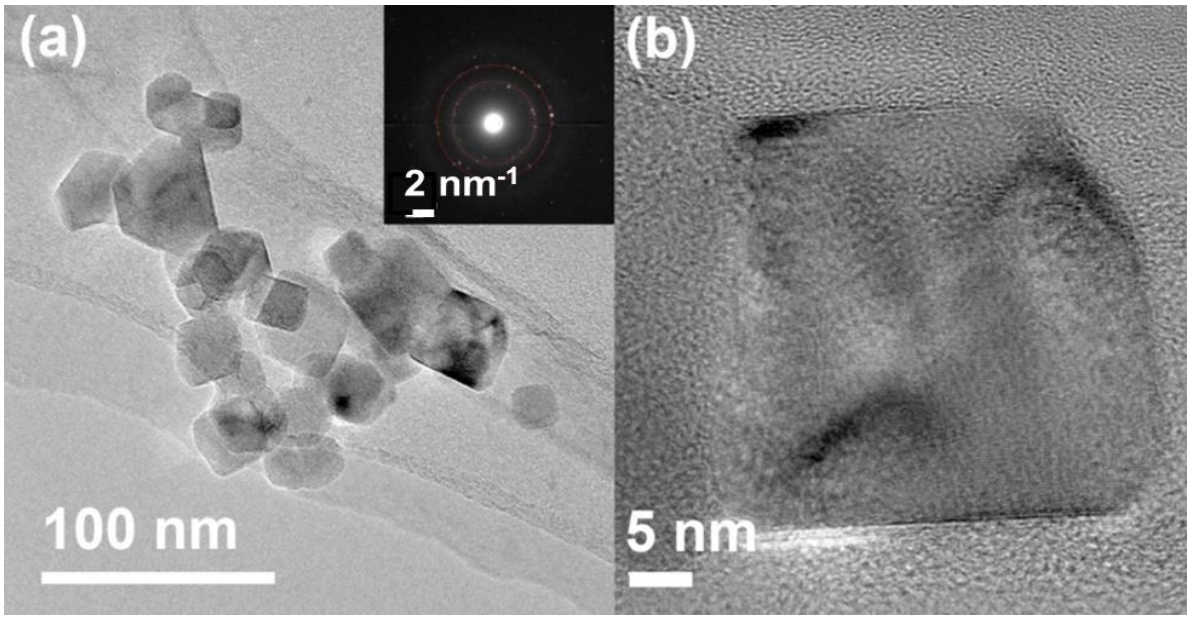

Figure S4. TEM images of powder particles treated at 800 °C for 6 hours. a) HRTEM image of the particles. The inset is the corresponding electron diffraction pattern. The d spacings of the rings (marked) match those of MgO; b) a single MgO particle.

As determined by elemental analysis and TGA, the MgO weight content of the material is around 14-18 wt.% giving a stoichiometric MgO content of around 32-46 mol.%. In TEM experiments there is a risk that the electron beam may cause $MgCO_3$ to decompose into MgO. To ensure that the observed MgO nanocrystals were not caused by the electron beam we gradually increasing the beam intensity whilst monitoring the TEM image of the sample, no changes to the sample were observed. No changes to the sample were observed even after prolonged beam exposure at 200 kV. These findings indicated that the MMC powder was stable under the conditions used to perform the TEM analysis.

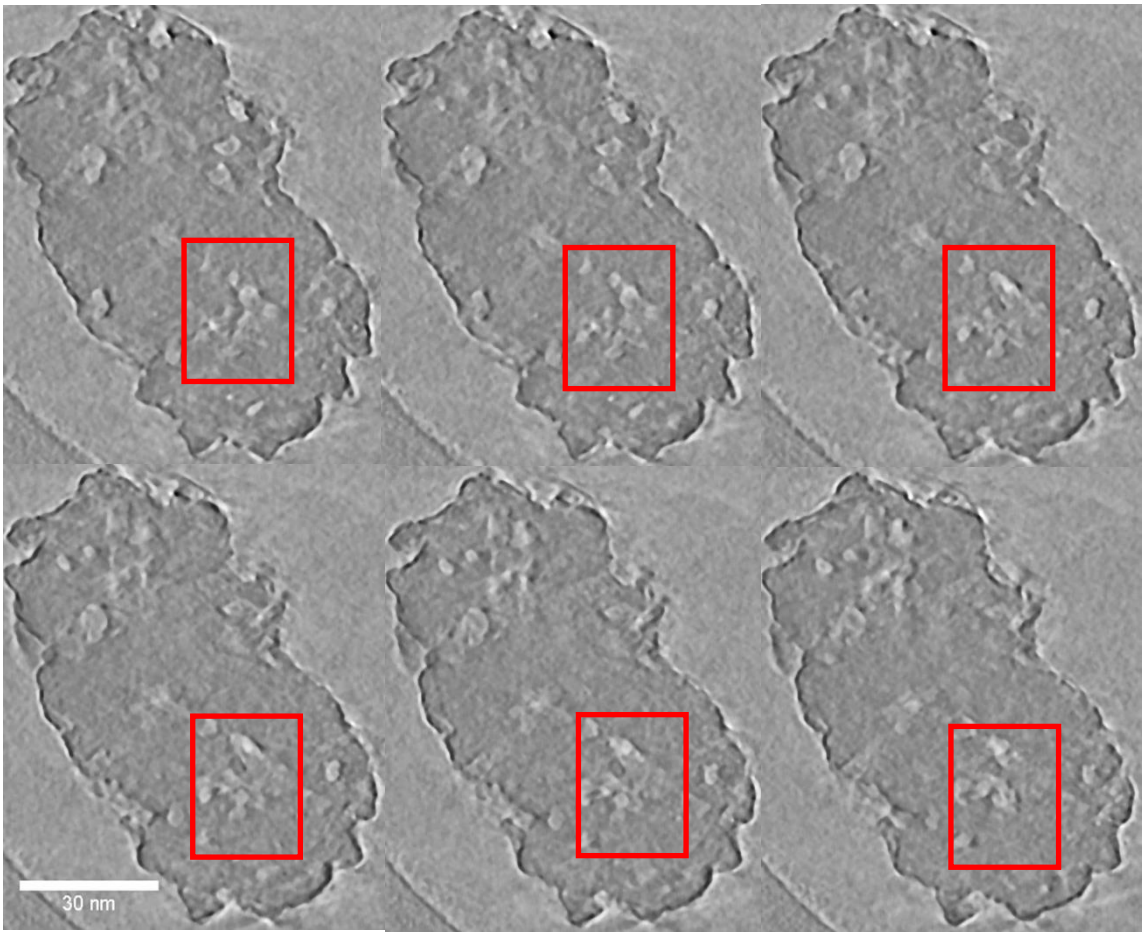

Figure S5. Six consecutive slices covering a thickness of 2.5 nm obtained from the tomogram reconstructed from the tilt series of TEM imags.

IR spectroscopy data

An IR spectroscopy analysis of the transparent MMC powder shows that the IR bands related to $MgCO_3$ were present, Figure S6. The figure further shows that the most intense carbonate band is the asymmetric stretch (υ_3) that is centered at around 1420 cm^{-1}. Other bands shown in the figure include the symmetric stretching (υ_1) band at 1097 cm^{-1} and the carbonate out of plane bending (υ_2) band at 857 cm^{-1}. The weak broad band at around 670 cm^{-1} is related to carbonate in plane bending (υ_4). A broad band related to hydrogen-bonded OH groups was also observable at around 3500 – 2800 cm^{-1}. This broad band remained clearly observable even when the sample was heated up to 250 °C using *in situ* IR microscopy setup, Figure S7. The presence of OH groups on the transparent powder material may be related to hydrogenated species as discussed earlier.

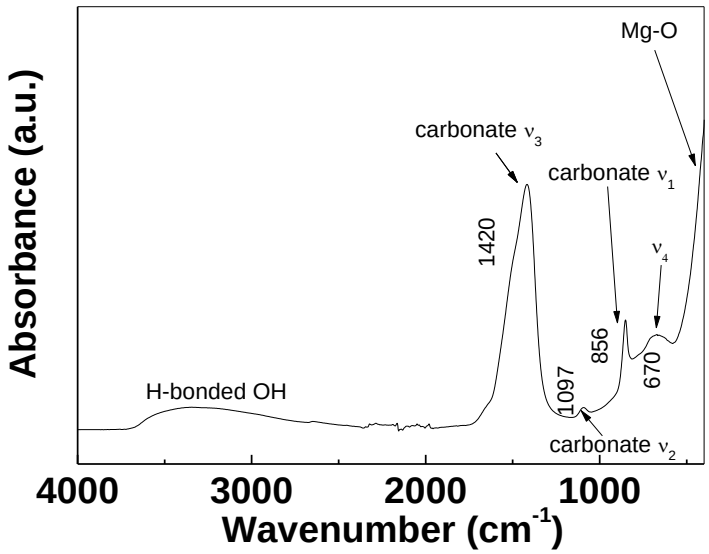

Figure S6. IR spectrum of dried transparent powder.

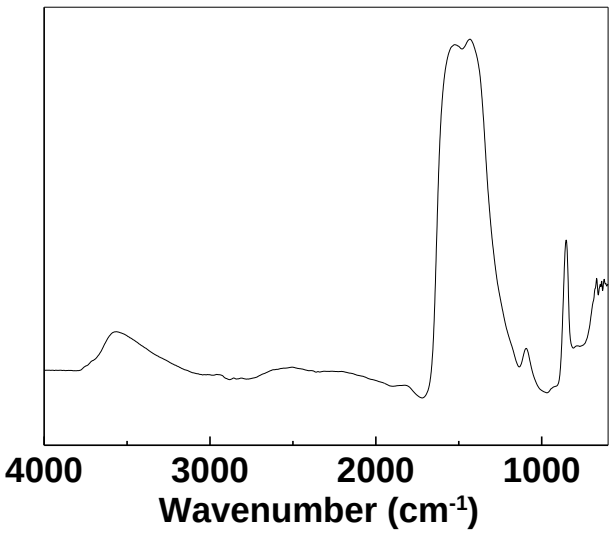

Figure S7. IR spectrum of transparent powder heated to 250 °C under nitrogen atmosphere.

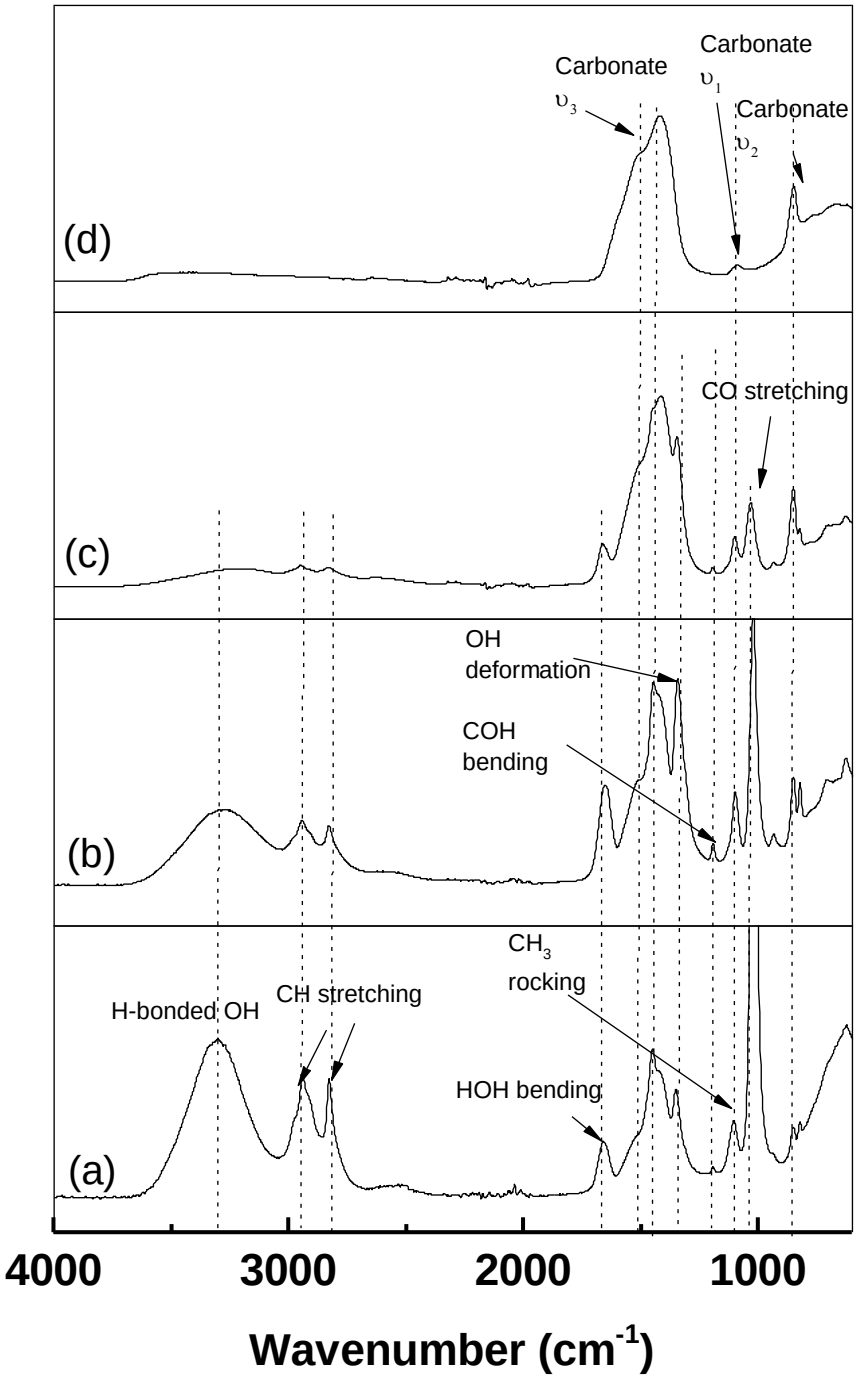

Figure S8. IR spectra of a) transparent reaction mixture, b) gel, c) wet powder and d) dried transparent powder.

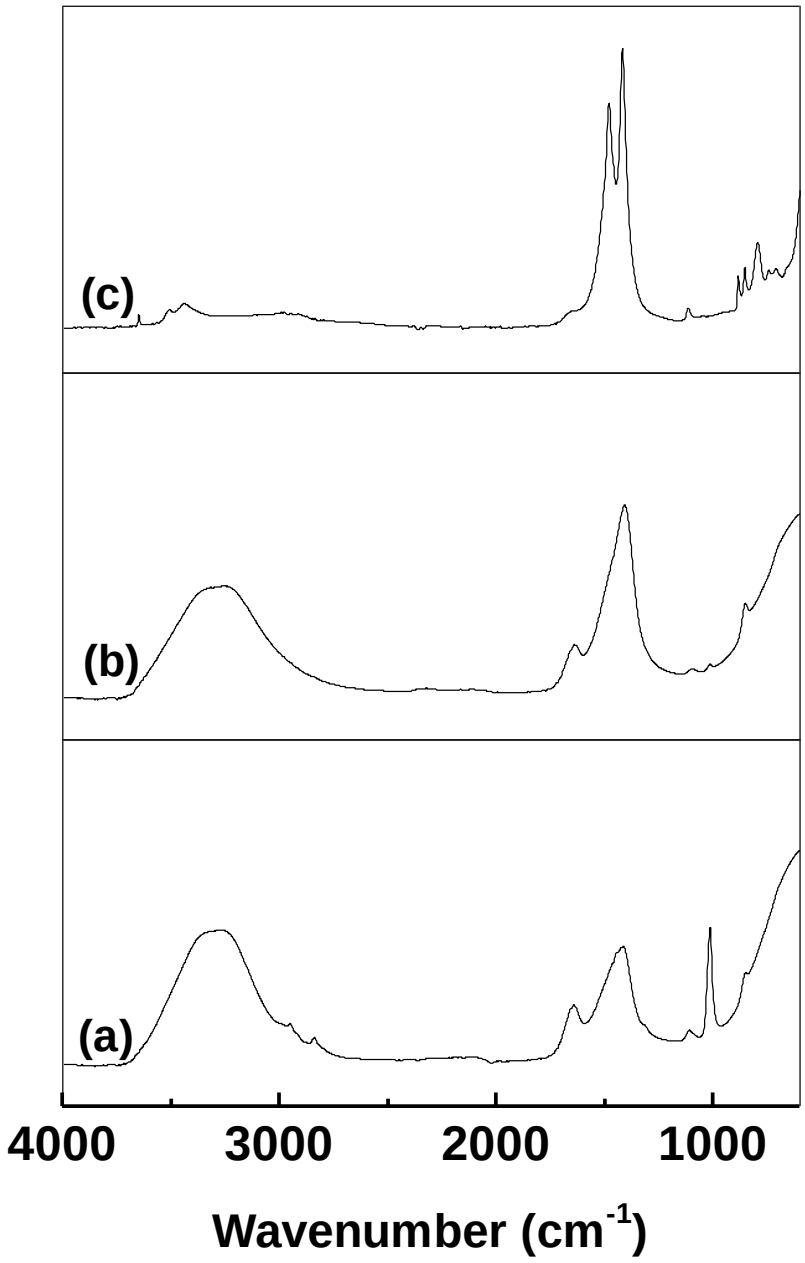

Figure S9. IR spectra visualizing the powder formation process when 30 vol.% of water is added to the reaction mixture. a) the reaction mixture with 30 vol.% water, b) the corresponding gel, c) the resulting powder after drying at 80 °C and thereafter at 150 °C, note that the carbonate bands are sharper than those shown in Figure S8d. The sharper bands indicate crystallinity, which is further confirmed by the presence of the antisymmetric carbonate band at around 750 -700 cm^{-1}, which is not observable in amorphous magnesium carbonate. The resulting material has low surface area and does not provide nitrogen sorption isotherms typical for a porous solid.

Table S3. IR band assignation of spectra recorded during different stages of the synthesis

Liquid	Gel	Solid, uncalcined	Solid, calcined	Vibration	Reference
851	851			Carbonate out of plane bending (ν_2)	[1-3]
1021	1021			CO stretching (methanol)	[4, 5]
1104	1101	1101	1095	Carbonate symmetric stretching (ν_1), superimposed by a CH_3 band (possibly rocking mode) in the case of liquid, gel and uncalcined solid	[1, 4-6]
1193	1192	1194	/	Assigned to COH bending mode	[5]
1351	1343	1347 ~1400-1600 1658	/ ~1400-1600 /	OH deformation mode of methanol	[4, 5]
~1400-1600	~1400-1600			Carbonate asymmetric stretching (ν_3)	[1, 6]
1659	1652			HOH bending (from adsorbed water)	[7]
2829/2940	2830/2943	2835/2953		CH stretching of methanol	[7]
3050-3600	3050-3620	~3000-3600		H-bonded OH vibration	[4, 7]

Total X-ray scattering and PDF analysis

The neighboring distance calculated from the PDF data matched that of the Mg-O bond in cubic magnesium oxide (2.10 Å).[8, 9] The other nearest neighbor distances aligned with those earlier seen for hydrated amorphous magnesium carbonate (AMC).[10]

Figure S8 shows the PDF of the oxide free transparent powder. The nearest neighbor distances that could be clearly assigned were C-O (at 1.27 Å) of carbonate, Mg-O (at 2.10 Å), Mg-Mg and O-O (3.02 Å) of cubic MgO.

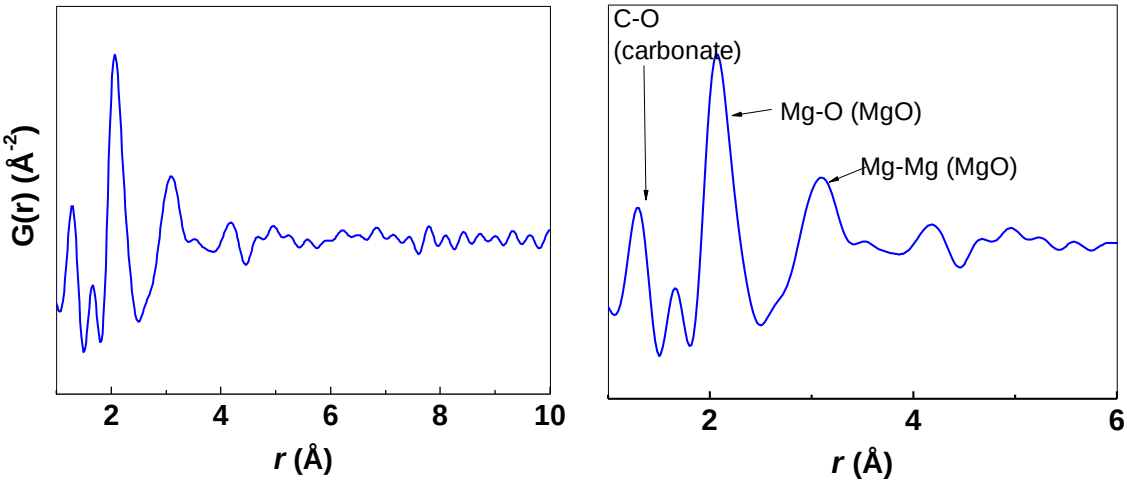

Figure S10. Pair distribution function analysis of the powder (left) and an enlarged version of the PDF (right) with some of the nearest neighbor distances labeled.

XPS analysis

XPS was used to examine the surface of the transparent powder, Figure S10. The Mg_{2p} and O_{1s} XPS spectra show that the surface of the powder particles contains mainly $MgCO_3$ and a small amount of MgO. The peaks for $MgCO_3$ were located at 52.5 eV for Mg_{2p} and at 534.1 eV for O_{1s},[11] they shifted slightly from those presented in our earlier study.[12] The small shift was most likely due to charging effects of the non-conducting sample.

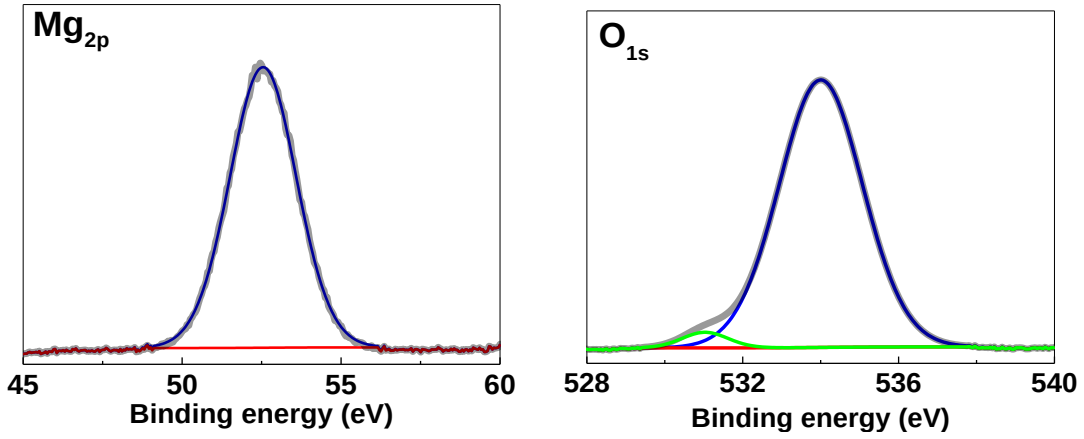

Figure S11. XPS spectra for Mg_{2p} and O_{1s}, for transparent MMC powder. In the Mg_{2p} spectrum the blue line for the magnesium carbonate fit is completely covered by the black line for the recorded spectrum, indicating an excellent fit.

Tyndal scattering/ Dynamic light scattering (DLS)

When the reaction vessel was pressurized with CO_2 (4 bar) for 24 hours, the reaction mixture became light yellow and only slightly cloudy. After centrifugation, the reaction mixture was an optically clear, yellow solution. DLS experiments revealed the presence of nanoparticle in the optically clear solution. DLS was employed to follow the behavior of the observed nanoparticles upon gel drying. Figure S11 shows the Z-average response of the reaction mixture immediately after centrifugation. As discussed in the main text, these nanoparticles grew with time due to aggregation (Figure S12). Tyndall scattering (Figure S12, photograph) was observed by shining red laser light through the solution, indicating the presence of nanoparticles being either MgO crystals, or $MgO/MgCO_3$ nanometer-sized composite particles in accordance with the HRTEM observations.

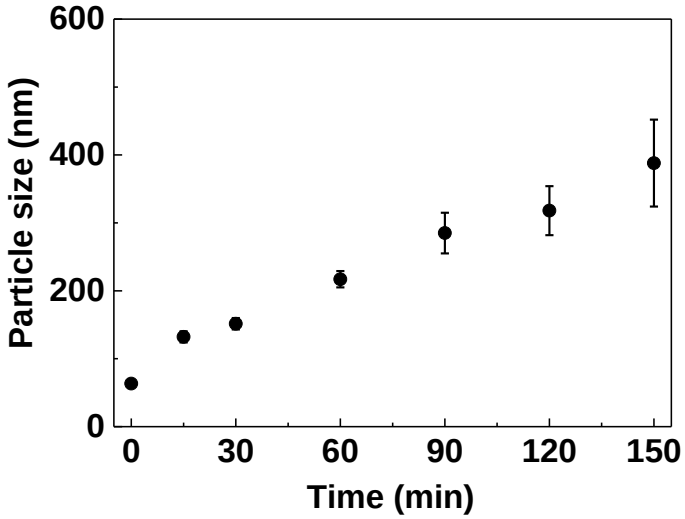

Figure S12. Particle size of the nanoparticles in the reaction mixture after centrifugation detected by dynamic light scattering. The nanoparticles grew in size with time, after 120 min the particles became too large to be detected.

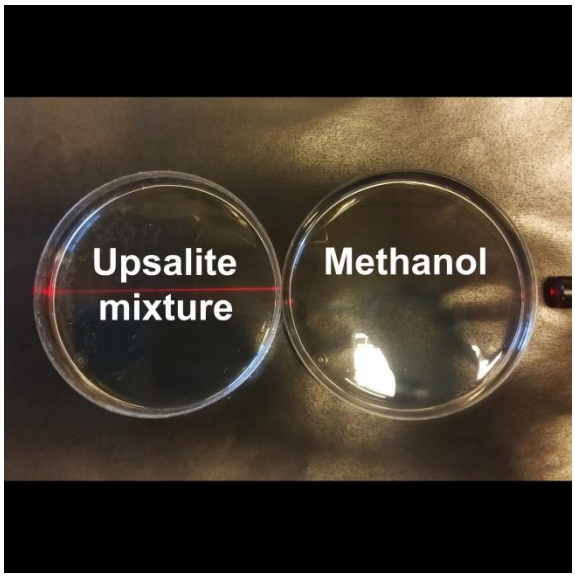

Figure S13. The observed Tyndall scattering on the reaction mixture.

N_2 sorption isotherm analysis

Figures S13-19 show adsorption isotherms and pore size distributions of the material with different average pore sizes. The pore size distributions were obtained by density functional theory (DFT) analysis.

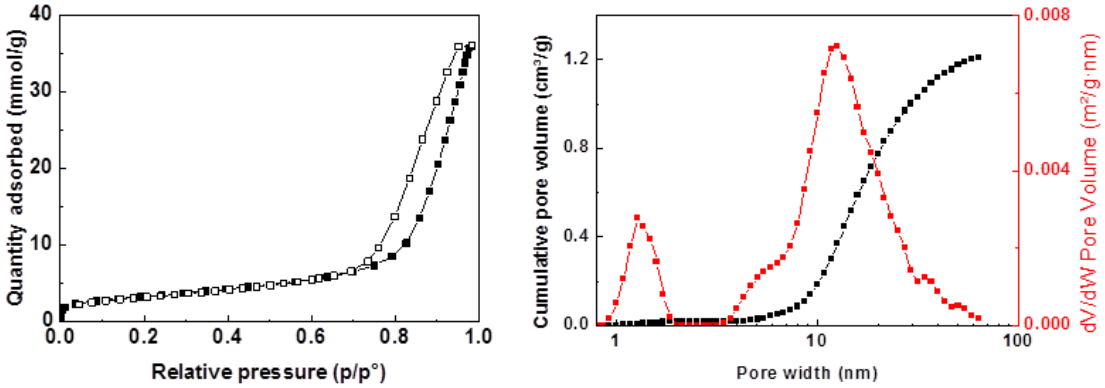

Figure S14. (left) N_2 adsorption isotherm and (right) DFT pore size distribution and cumulative pore volume of sample A as listed in the main text.

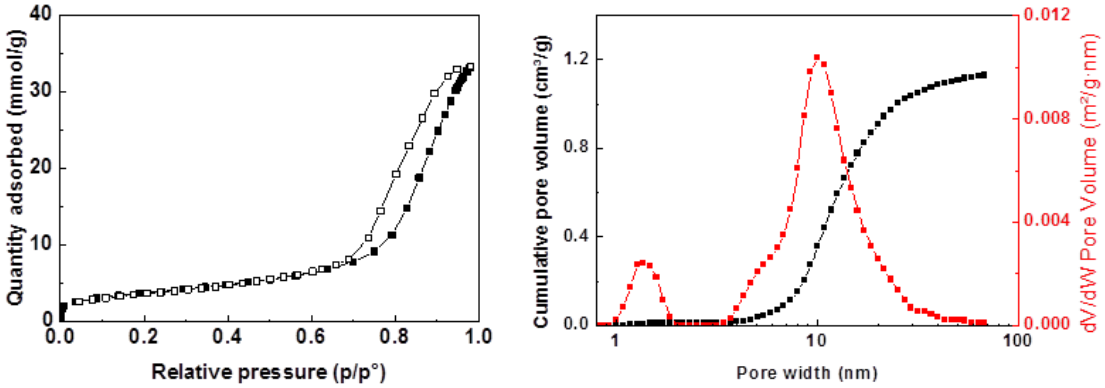

Figure S15. (left) N_2 adsorption isotherm and (right) DFT pore size distribution and cumulative pore volume of sample B as listed in the main text.

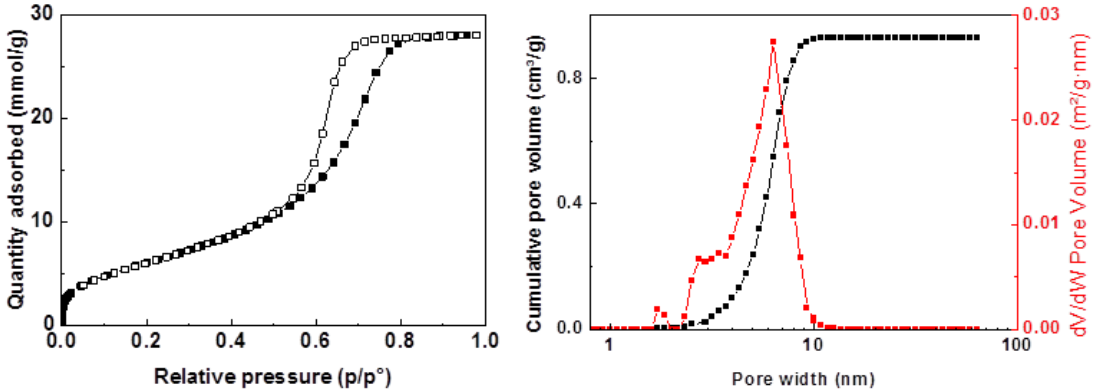

Figure S16. (left) N_2 adsorption isotherm and (right) DFT pore size distribution and cumulative pore volume of sample C as listed in the main text.

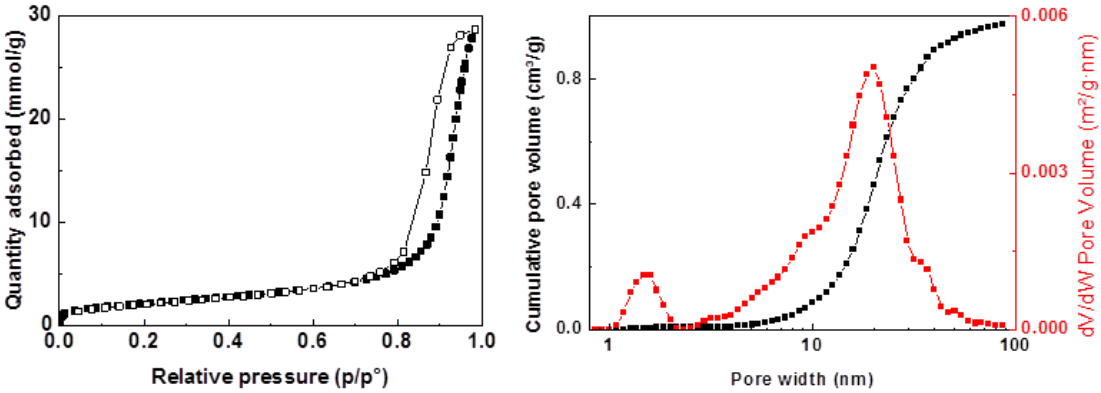

Figure S17. (left) N_2 adsorption isotherm and (right) DFT pore size distribution and cumulative pore volume of sample D as listed in the main text.

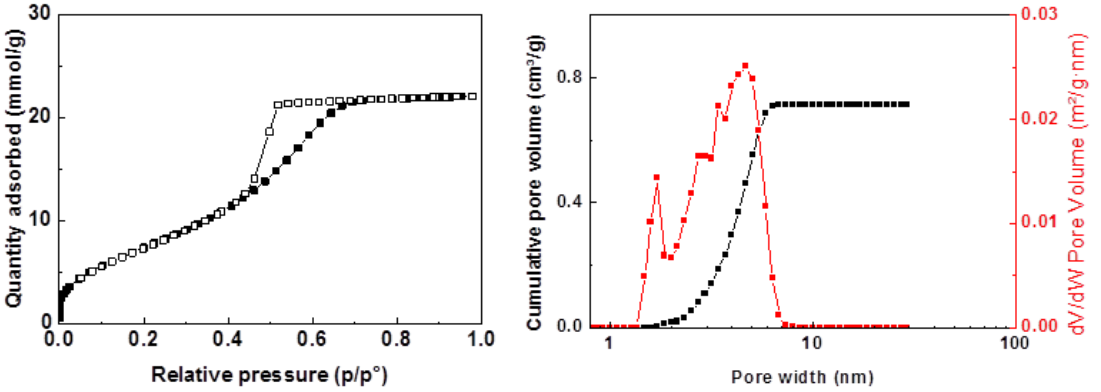

Figure S18. (left) N_2 adsorption isotherm and (right) DFT pore size distribution and cumulative pore volume of sample E as listed in the main text.

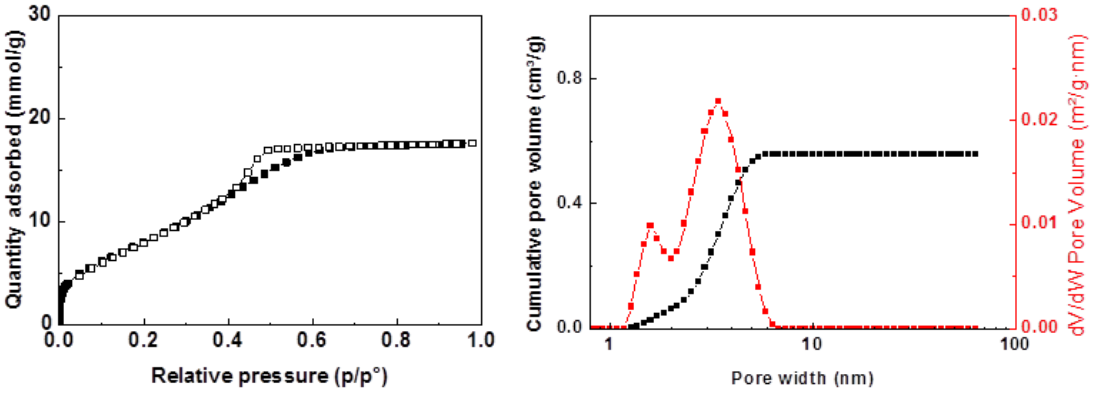

Figure S19. (left) N_2 adsorption isotherm and (right) DFT pore size distribution and cumulative pore volume of sample F as listed in the main text.

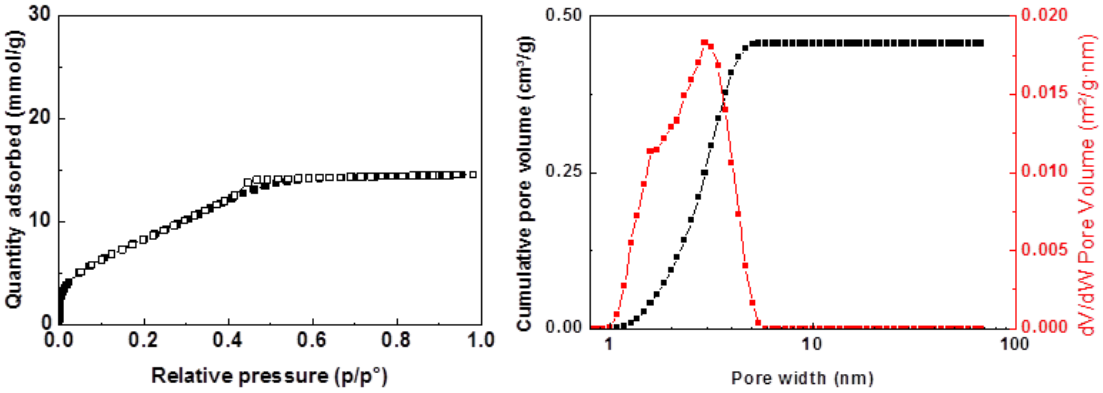

Figure S20. (left) N_2 adsorption isotherm and (right) DFT pore size distribution and cumulative pore volume of sample G as listed in the main text.

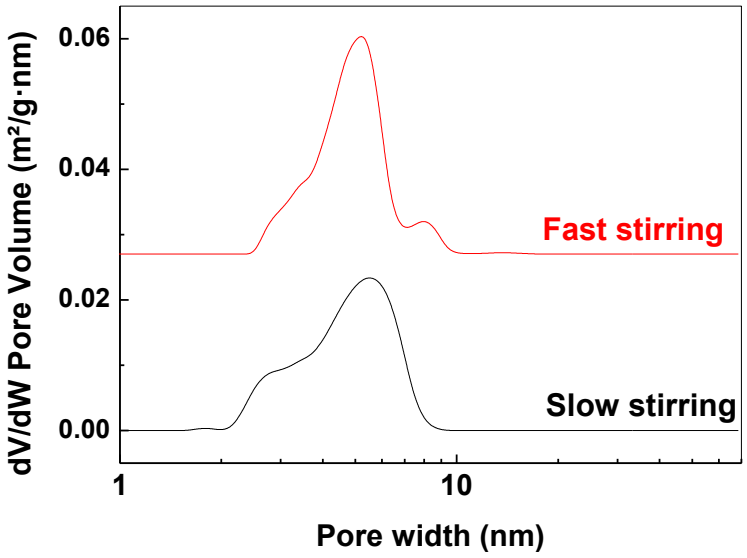

Figure S21. The effect of stirring rate on the pore size of MMC prepared by powder formation at 30 °C. Two stirring speeds were employed: fast stirring at 125 rpm and slow stirring at 50 rpm, significant differences were not noted using our experimental setup

Delivery of itraconazole from transparent MMC with different pore sizes

Differential scanning calorimetry (DSC) was employed to analyze the structure of ITZ loaded into the pores of the transparent MMC and the curves recorded for the three different concentrations of drug loaded into the samples with varying average pore sizes as well as for the pure drug are displayed in Figure S20.

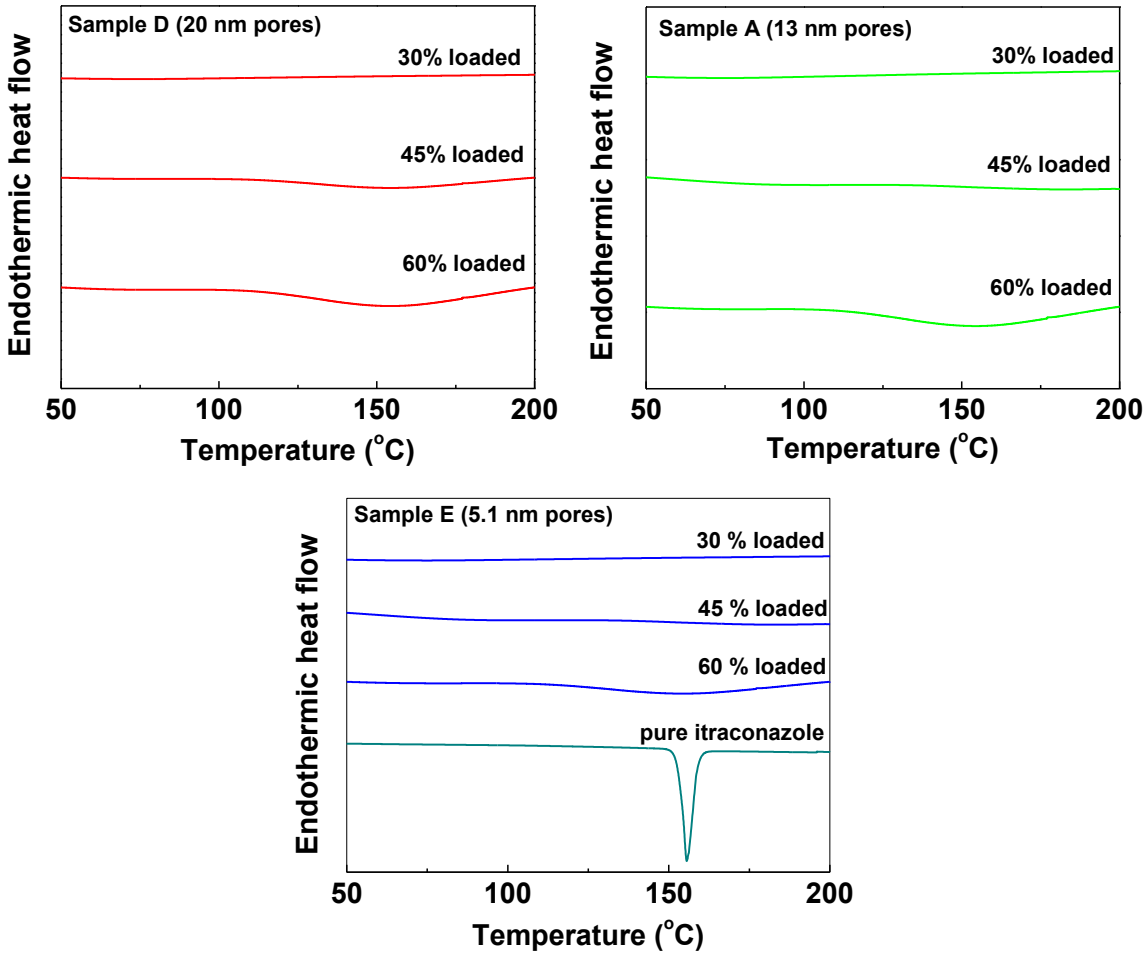

Figure S22. DSC curves of ITZ loaded transparent MMC for the three different concentrations of drug loaded into the samples with varying average pore sizes as well as for the pure drug.

Table S4. DSC analysis of MMC with different average pore sizes loaded with different amounts of itraconazole.

	Average pore size (nm)	30 % loading	45 % loading	60 % loading
Sample D	~20	amorphous	semi-crystalline	semi-crystalline
Sample A	~13	amorphous	amorphous	semi-crystalline
Sample E	~5.1	amorphous	amorphous	semi-crystalline

References

1. D. Gebauer, P. N. Gunawidjaja, J. Y. P. Ko, Z. Bacsik, B. Aziz, L. Liu, Y. Hu, L. Bergström, C.-W. Tai, T.-K. Sham, M. Edén and N. Hedin, *Angew. Chem., Int. Ed.*, 2010, **49**, 8889-8891.
2. F. A. Andersen and L. Brecevic, *Acta Chem. Scand.*, 1991, **45**, 1018-1024.
3. J. D. Baxter, R. M. Biltz and E. D. Pellegrino, *Yale J. Biol. Med.*, 1966, **38**, 456-470.
4. R. Kagel and R. G. Greenler, *J. Chem. Phys.*, 1968, **49**, 1638-1647.
5. T. Iwasita and F. Nart, *J Electroanal. Chem. Interfacial Electrochem.*, 1991, **317**, 291-298.
6. F. A. Andersen and L. Brecevic, *Acta Chem. Scand*, 1991, **45**, 1018-1024.
7. D. H. Williams and I. Fleming, *Spectroscopic Methods in Organic Chemistry*, McGraw-Hill, 1995.
8. T. Guerra and I. Borges, *J. Chem.*, 2013, **2013**, 8.
9. A. F. Wells, *Structural inorganic chemistry*, Oxford University Press, 2012.
10. C. E. White, N. J. Henson, L. L. Daemen, M. Hartl and K. Page, *Chem. Mater.*, 2014, **26**, 2693-2702.
11. M. Santamaria, F. Di Quarto, S. Zanna and P. Marcus, *Electrochim. Acta*, 2007, **53**, 1314-1324.
12. J. Forsgren, S. Frykstrand, K. Grandfield, A. Mihranyan and M. Strømme, *PLoS One*, 2013, **8**, e68486.